CrossMark

ORIGINAL PAPER

An Experimental and Numerical Study on Mechanical Behavior of Ubiquitous-Joint Brittle Rock-Like Specimens Under Uniaxial Compression

Ri-hong Cao[1] · Ping Cao[1] · Xiang Fan[2] · Xinguang Xiong[1] · Hang Lin[1]

Abstract Rock engineers often encounter materials with a large number of discontinuities that significantly influence rock stability. However, the strength and failure patterns of ubiquitous-joint rock specimens have not been examined comprehensively. In this study, the peak uniaxial compressive strength (UCS_J) and failure patterns of ubiquitous-joint rock-like specimens are investigated by combining similar material testing and numerical simulation using the two-dimensional particle flow code. The rock-like specimens are made of white cement, water, and sand. Flaws are created by inserting mica sheets into the fresh cement mortar paste. Under uniaxial compressional loading, the failure patterns of ubiquitous-joint specimens can be classified into four categories: stepped path failure, planar failure, shear-I failure, and shear-II failure. The failure pattern of the specimen depends on the joint-1 inclination angle α and the intersection angle γ between joint-1 and joint-2, while α strongly affects UCS_J. The UCS_J of specimens with $\gamma = 15°$ or $30°$ shows similar tendencies for $0° \leq \alpha \leq 75°$. For specimens with $\gamma = 45°$ or $60°$, UCS_J increases for $0° \leq \alpha \leq 30°$ and decreases for $\alpha > 30°$. For specimens with $\gamma = 75°$, the UCS_J peaks when $\alpha = 0°$ and increases for $60° \leq \alpha \leq 75°$. The numerical and experimental results show good agreement for both the peak strength and failure patterns. These results can improve our understanding of the mechanical behavior of ubiquitous-joint rock mass and can be used to analyze the stability of rock slopes or other rock engineering cases such as tunneling construction in heavily jointed rock mass.

1 Introduction

Joints, fissures, and weak surfaces are common in natural rocks. When a load is applied, new cracks develop near the tips of existing joints and may propagate or coalesce with other cracks. The propagation of new cracks and the coalescence of fractures lead to a degradation in the mechanical properties of the rock. In some cases, this will result in rock mass failure, a topic that has received much attention in rock mechanics and rock engineering.

Previous studies (Vallejo 1988; Vallejo et al. 2013; Dyskin et al. 2003; Hoek and Bieniawski 1965; Li et al. 2005; Park and Bobet 2009; Cao et al. 2015; Yang et al. 2013; Sagong and Bobet 2002; Tang et al. 2001; Wong 2008; Wong and Chau 1998 and so on) of crack coalescence between fractures utilized laboratory tests because of the difficulties of in situ tests. With recent rapid developments in computer science, many numerical methods have been suggested to simulate crack initiation and coalescence; most of the simulation results show good agreement with experimental results. For specimens that contain a single fracture, two types of cracks can develop from the tips of the existing fracture: wing cracks and secondary cracks. A wing crack is a tensile crack that originates from the tip of the fissure and propagates at an

✉ Ping Cao
caowei198804@126.com

[1] School of Resources and Safety Engineering, Central South University, Changsha 410083, Hunan, China

[2] School of Highway, Chang'an University, Xi'an 710064, China

angle toward the direction of maximum compression, whereas a secondary crack is a shear crack (Shen 1995; Sahouryeh et al. 2002; Dyskin et al. 2003; Li et al. 2005; Wong and Einstein 2006; Park and Bobet 2010; Yang et al. 2012; Cao et al. 2015).

For a specimen containing two or three fractures, previous studies focused on crack coalescence between parallel fractures (Vallejo 1987; Bobet and Einstein 1998b; Li et al. 2005; Wong and Li 2013; Park and Bobet 2009; Sagong and Bobet 2002; Tang et al. 2001; Vasarhelyi and Bobet 2000; Wong 2008; Wong and Chau 1998; Wong et al. 2001; Yang 2011; Zhang and Wong 2013a, b; Zhou and Yang 2007; Zhou et al. 2014, 2015; Vallejo 1989). Significant advances were achieved in understanding the coalescence pattern between parallel fractures. There are mainly three types of failure modes for these specimens: tensile failure, shear failure, and mixed failure.

In addition to studies on parallel fractures, the mechanical properties and penetration mode of un-parallel fractures in a specimen are also well discussed in the literature. Combining numerical simulation using the two-dimensional particle flow code (PFC2D) and un-parallel fissures experiments using PMMA, Hwangdeung granite, and Diastone, Lee and Jeon (2011) investigated the penetration mode between two un-parallel fissures. Based on parallel bonded-particle models, Zhang et al. (2015a, b) studied crack coalescence between two non-parallel flaws and observed five types of linkage between two flaws: tensile crack linkage, tensile crack linkage with shear coalescence at the tip, shear crack linkage, mixed linkage, and indirect crack linkage. Using photographic monitoring and acoustic emissions monitoring techniques, Yang et al. (2013) investigated the relationship between the real-time crack coalescence process and axial stress–time behavior for red sandstone containing two un-parallel fissures.

While previous work has promoted the understanding of crack propagation, coalescence, and failure modes of brittle materials with fissures, the strength and failure patterns of ubiquitous-joint rock specimens have not been studied comprehensively. Compared with specimens containing one, two, or three fissures, the mechanical behaviors of those with multiple flaws or joints are expected to be more complicated. In practical engineering, the rock mass usually contains multiple joints. The number of joints will increase in the case of ubiquitous-joint rock mass (Fig. 1). Both the inclination and intersection angles between two set of joints affect the mechanical properties and failure mode of rock mass. In this paper, we combine experiments using rock-like material and a discrete element numerical method (PFC2D) to investigate the mechanical behavior and failure mode of ubiquitous-joint rock-like materials.

Fig. 1 Idealized schematic showing the ubiquitous-joint rock mass

2 Experimental Studies

2.1 Specimen Preparation

As mentioned above, laboratory tests have been widely used as an effective research method for crack coalescence between fractures in brittle materials. So far, many types of materials have been employed for such tests, including glass (Hoek and Bieniawski 1965), Columbia Resin 39 (Bombolakis 1968), and molded gypsum (Park 2001; Shen 1995; Bobet and Einstein 1998a, b; Reyes and Einstein 1991; Sagong and Bobet 2002; Wong and Einstein 2009a, b).

Because the main framework of the rock consists of mineral grains and silicon or argillaceous material between the grains, friction will increase in the failure plane when the specimens fail. This friction will then affect the strength of the specimens. Therefore, we selected cement mortar as the rock-like material for our experiment. The grains in the specimen are sand, which provides the frictional behavior of the modeling material. The adhesive material between the grains is cement.

The rock-like specimens are made of white cement, water, and sand. The volume proportions $V_{water}:V_{white\ cement}:V_{silica\ sand}$ in the specimens are 1:1:2. The dimensions (height × width × thickness) of each specimen are $200 \times 150 \times 30$ mm. The existing fissures were created by inserting mica sheets (0.6 mm thick, 30 mm long) into the fresh cement mortar paste at the desired location of the fissures; the sheets were not removed before the modeling material set. The specimens were removed from the mold and soaked in water for 3 days. They were placed inside a standard curing box (with the temperature controlled at 20 ± 2 °C and humidity controlled at 80 %) for 25 days before being subjected to mechanical testing. The average values of the unit weight (γ_m), Young's modulus (E_m), uniaxial compressive strength (UCS), and Poisson's ratio (v) of

Fig. 2 Schematics of joint geometry configurations in the blocks. α: joint-1 orientation with respect to horizontal. β: joint-1 orientation with respect to horizontal γ: $\beta - \alpha$. **a** Joint-1, **b** joint-2, and **c** jointed model
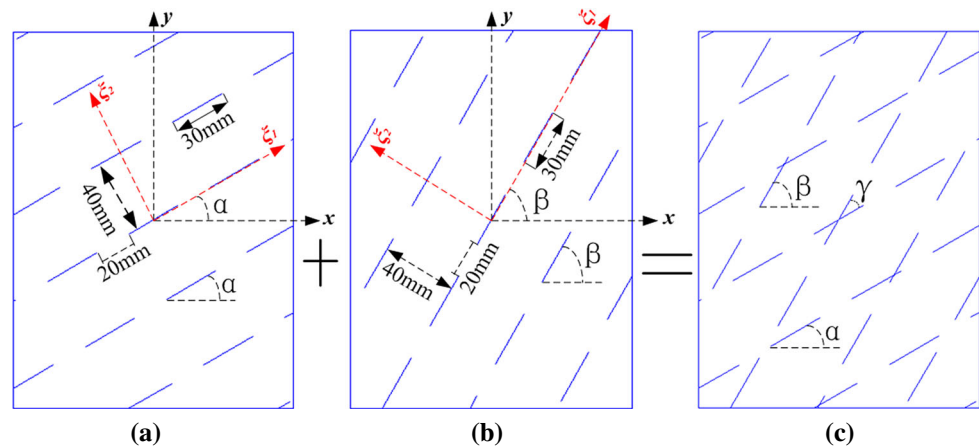
α:joint1 orientation with respect to horizontal β :joint1 orientation with respect to horizontal γ: $\beta - \alpha$

the rock material are γ_m = 2.159 g/cm^3, E_m = 3.242 GPa, UCS = 8.01 MPa, and v = 0.2371.

The joint geometry is defined by two geometrical parameters as shown in Fig. 2: joint-1 with an inclination angle α (Fig. 2a) and intersection angle γ ($\beta - \alpha$) (Fig. 2c). The ubiquitous-joint rock-like specimens are created with various combinations of joint-1 and joint-2 angles. The experiments were performed for specimens with five different α values of joint-1: 0°, 30°, 45°, 60°, and 75°, while joint-2 revolved around the z-axis counterclockwise in increments of 15° until γ reached 75°.

Table 1 shows the fissure geometry information for all the specimens in this study. Each specimen was assigned an ID number using the notation S-a-b, where S stands for the sample, 'a' represents the angle of joint-1 in degrees, and b is the intersection angle γ in degrees. Figure 3 shows the joint geometry configurations generated for α = 30° (S-30-15, S-30-30, S-30-45, S-30-60, S-30-75).

Table 1 Sample numbers and fissure geometrical parameter values used for all specimens

| Number	Specimen ID	α	γ	Number	Specimen ID	α	γ
1	S-0-15	0	15	14	S-45-60	45	60
2	S-0-30	0	30	15	S-45-75	45	75
3	S-0-45	0	45	16	S-60-15	60	15
4	S-0-60	0	60	17	S-60-30	60	30
5	S-0-75	0	75	18	S-60-45	60	45
6	S-30-15	30	15	19	S-60-60	60	60
7	S-30-30	30	30	20	S-60-75	60	75
8	S-30-45	30	45	21	S-75-15	75	15
9	S-30-60	30	60	22	S-75-30	75	30
10	S-30-75	30	75	23	S-75-45	75	45
11	S-45-15	45	15	24	S-75-60	75	60
12	S-45-30	45	30	25	S-75-75	75	75
13	S-45-45	45	45				

2.2 Equipment

Figure 4 shows the compression test setup. The specimen was placed between the two loading platforms in the servo control uniaxial loading instrument, and the loading was controlled by the loading control system (DCS-200). The loading rate was 0.3 mm/min. The top and bottom boundaries are fixed in the horizontal direction. To reduce the end effect, the contact area between the specimen and the loading platform was coated with butter. The specimens were loaded under compression until failure, and the failure process was recorded by a video camera.

## 2.3 Failure Model of a Multi-fissure Specimen

Previous experimental and numerical results showed that when a load is applied to specimens with a single fissure, three types of cracks develop from the pre-existing fissure (Fig. 5): wing cracks, quasi-coplanar secondary cracks, and oblique secondary cracks (Shen 1995; Sahouryeh et al. 2002; Li et al. 2005; Wong and Einstein 2006; Park and Bobet 2010; Yang et al. 2012; Cao et al. 2015).

For ubiquitous-joint specimens, the mechanical behavior will be more complicated. When compression is applied on the existing flaws, tensile or shear cracks will develop from the tips of the existing fractures. As loading continues, these cracks will propagate and join with other cracks, penetrating through the rock. Thus, the pre-existing fissures will join with neighboring cracks, resulting in various types of failure patterns. Based on experimental observations, the failure patterns of ubiquitous-joint rock-like specimens can be generally classified into four categories: (1) stepped path failure; (2) planar failure; (3) shear-I failure; and (4) shear-II failure.

Fig. 3 Ubiquitous-joint specimens with $\alpha = 30$. **a** Intact model, **b** S-30-15, **c** S-30-30, **d** S-30-45, **e** S-30-60, and **f** S-30-75
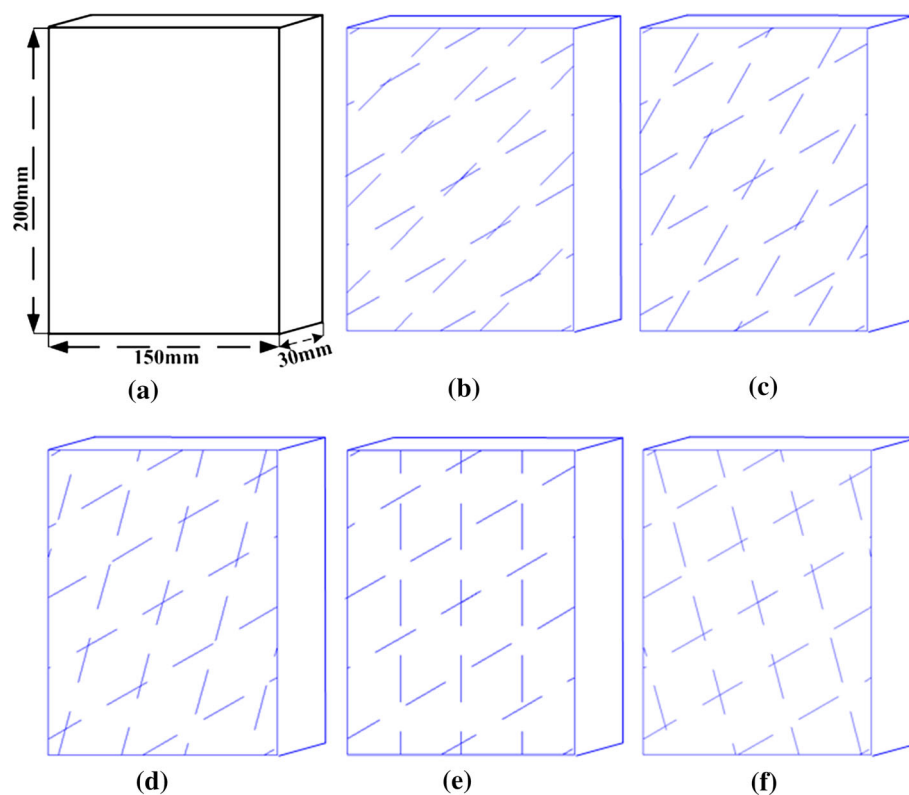
**Fig. 4** View of the specimens ready to be tested and the layout of the loading system
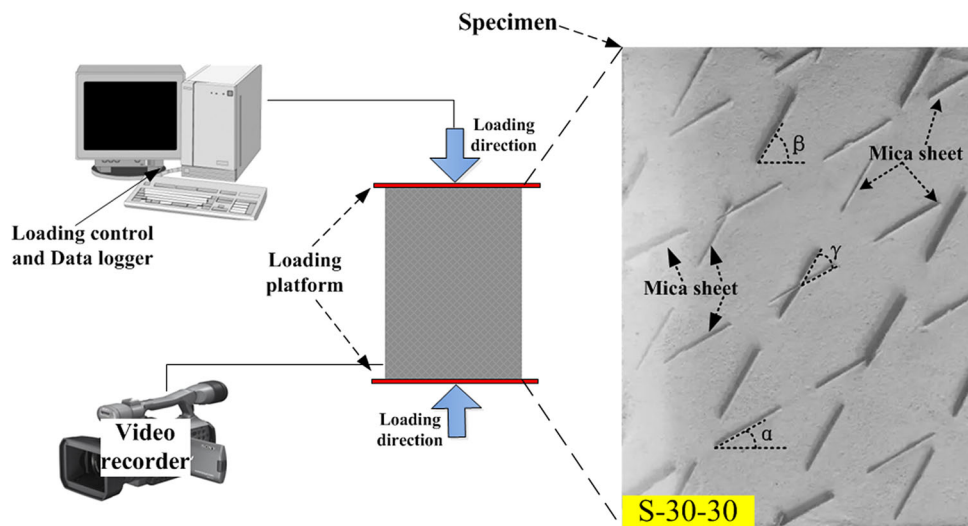
2.3.1 Stepped Path Failure

Specimen S-0-30 (Fig. 6) exhibits a typical stepped path failure pattern. In this type of failure mode, several 'stepped failure planes' occur in the specimen in various locations. The coalescence mode between the pre-existing flaws on the stepped failure planes is mainly tensile cracks. Under compression, tensile cracks develop from the pre-existing flaws and propagate along the direction of axial stress. With further loading, the tensile cracks join with other cracks, forming the observed coalescence.

In the failure pattern shown in Fig. 6, most of the cracks are approximately parallel to the loading direction. Notably, other cracks such as shear or mixed cracks appear besides the tensile cracks in the stepped path failure specimens.

2.3.2 Planar Failure

Specimen S-60-75 (Fig. 7) is a typical example of a planar failure pattern. Several coalescence modes appear between the pre-existing flaws (including tensile, shear, and mixed
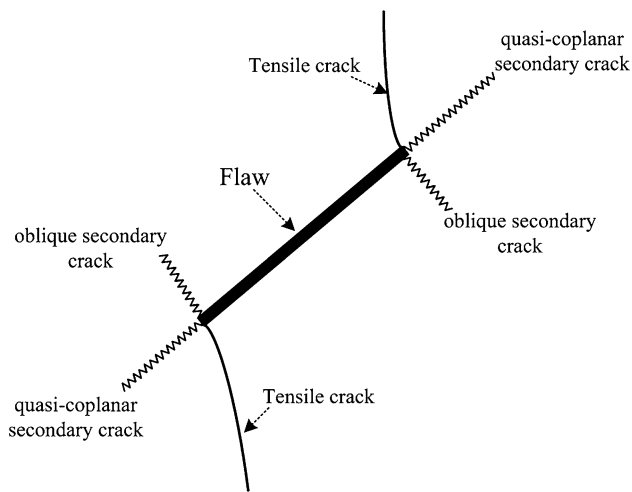
Fig. 5 Crack types observed in pre-flawed specimens under compression (Bobet 2000)

cracks). Most of the shear cracks between the pre-existing fissures are quasi-coplanar secondary shear cracks, which are similar to the category 4 coalescence discussed by Wong and Einstein (2009a).

In addition to shear cracks, some parallel and un-parallel flaws also connect with each other through tensile cracks. Under loading, tensile and shear cracks develop from the pre-existing flaws. As the loading continues, new cracks propagate and join with others and penetrate through the specimen. At the residual stage, the specimen appears fragmented—the pre-existing flaws and new cracks have split the specimen into many small blocks. Clearly, there are no far-field cracks seen in the specimen.
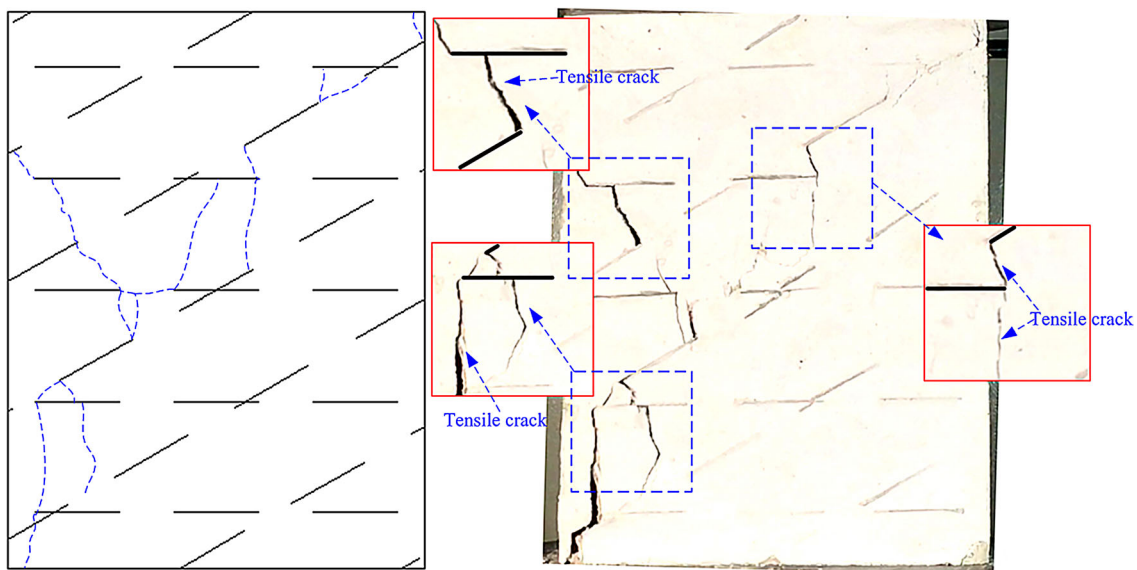
2.3.3 Shear Failure

The shear failure mode can be divided into two types based on the failure characteristics of the shear failure pattern: shear-I failure pattern and shear-II failure pattern.

2.3.3.1 Type I Shear Failure This pattern has either a single shear failure plane or a set of parallel shear failure planes. Specimen S-60-30 (Fig. 8) is a typical example of this failure pattern. The coalescence mode between the pre-existing flaws on the main failure plane comprises quasi-coplanar secondary shear cracks that correspond to category 4 coalescence according to Wong and Einstein (2009a). Under loading, shear cracks develop from the fissure tips; with further loading, the shear cracks propagate, joining with other shear cracks and penetrating through the specimen.

During failure, the specimen is split into two or three blocks by the parallel shear failure plane. The shear failure plane consists of quasi-coplanar secondary shear cracks and pre-existing flaws. Indentations and friction debris can be clearly seen on the surface of the failure plane. After the shear failure plane forms in the specimen, with further loading, tensile cracks continue to propagate until the specimen reaches the residual stage. As shown in Fig. 8, there are also some obvious tensile cracks in this pattern.

2.3.3.2 Type II Shear Failure Specimen S-60-60 (Fig. 9) is a typical example of the shear-II failure pattern. Compared with the parallel shear failure plane in the shear-I failure pattern, in this pattern, the specimen exhibits a set of cross-shear failure surfaces. The coalescence modes

Fig. 6 Crack coalescence in stepped path failure
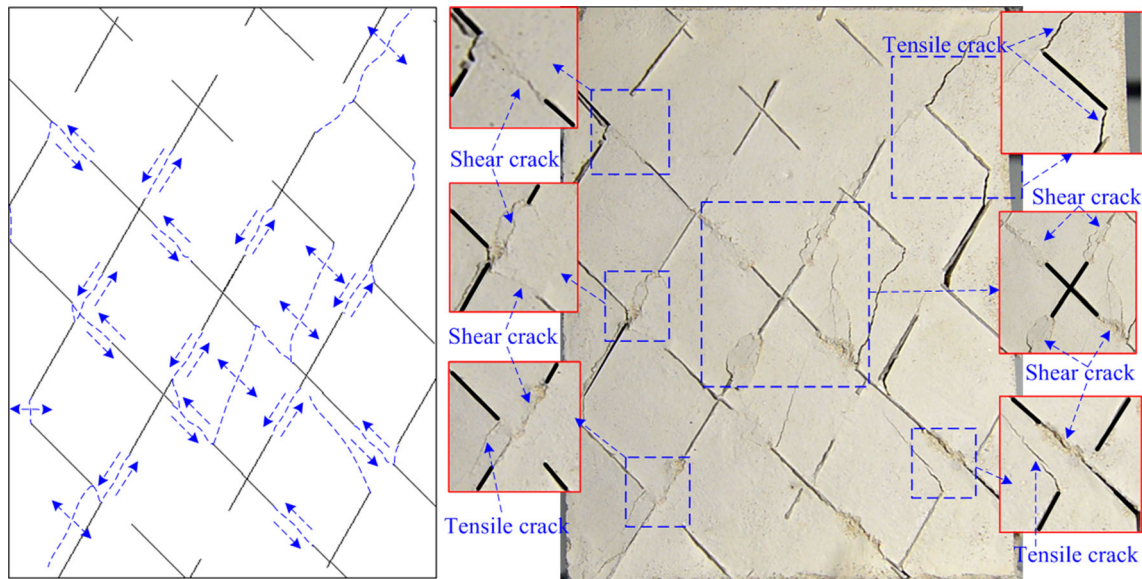
Fig. 7 Crack coalescence in planar failure
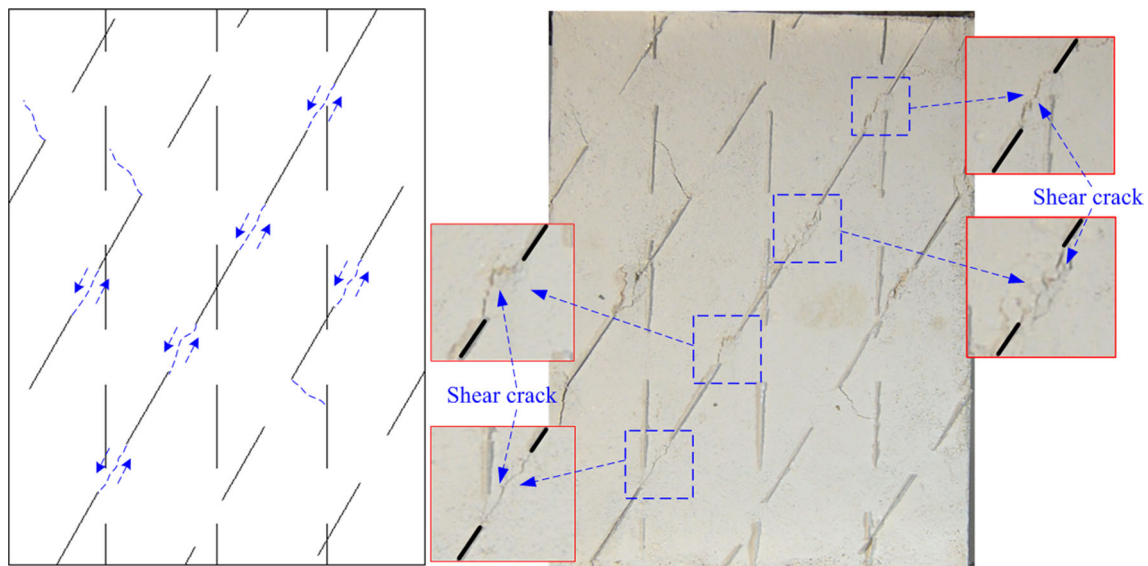
**Fig. 8** Crack coalescence in shear-I failure

between the pre-existing flaws on the cross-shear failure plane are shear cracks.

Under loading, shear cracks develop from the fissure tips. With further loading, new cracks propagate and join with neighboring cracks or pre-existing flaws to form a cross-shear failure surface. In Fig. 9, although some of the blocks fall outside the specimen, the cross-shear failure plane in the experimental result is very clear. As in the shear-I failure pattern, indentations and friction debris are clearly visible on the shear failure plane.

In this paper, the rock-like specimens are made of white cement, water, and sand. And the existing fissures

were created by inserting mica sheets (0.6 mm thick, 30 mm long) into the fresh cement mortar paste at the desired location of the fissures; the sheets were not removed before the modeling material set. Based on the experimental results, the cohesion (C_j) and friction angle (ϕ_j) between the cemented material and the mica sheets are 18.2 kPa and 11°, respectively. The C_j and ϕ_j values in our study are very close to those in Zhang et al. (2015a, b). Clearly, C_j and ϕ_j affect the initiation and coalescence stress. However, according to Park and Bobet (2009), 'the cracking pattern and the cracking processes that occur in specimens with closed flaws are the same as

Fig. 9 Crack coalescence in shear-II failure
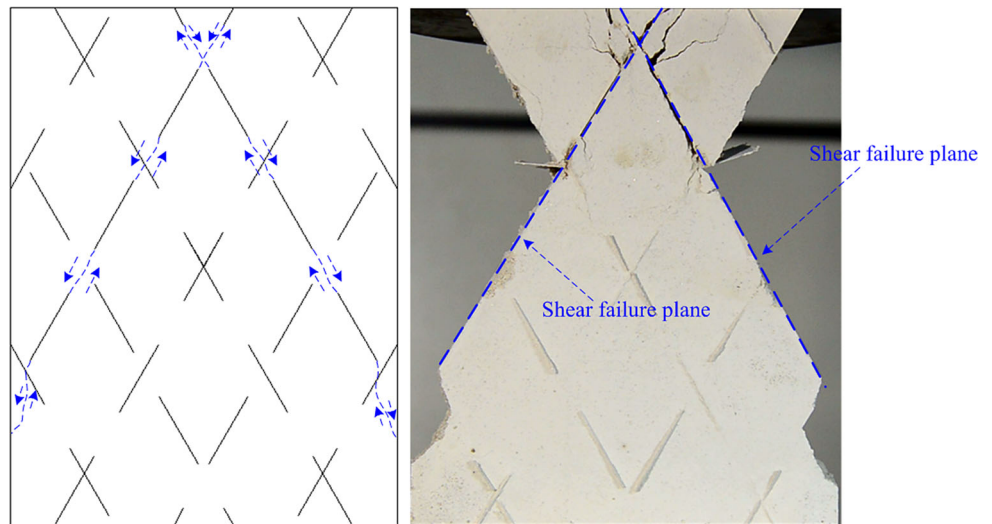
with open flaws, and so it is expected that the fracture mechanisms and principles that apply to both types of flaws are the same.' Moreover, based on XFEM, Xie et al. (2016) found that the initiation location and angle of the cracks are not influenced by friction. Because the friction angle between the cement and the mica sheet in this study is much smaller than that of the cement–cement face, therefore, we can assume that the friction angle between the cement and mica sheet has no considerable effect on the direction of propagation of the wing cracks or secondary cracks.

Table 2 summarizes the failure patterns of rock-like specimens containing multiple flaws with different α and γ values approximately at the residual strength. Specimens S-0-15, S-0-30, and S-30-15 underwent stepped path failure, with the failure of the specimen caused mainly by the propagation of tensile cracks. Specimens S-45-15, S-60-15, S-30-60, and S-30-75 show failure mode patterns between stepped path failure and shear-I failure; in these specimens, the pre-existing fissures are connected through tensile or coplanar shear cracks, resulting in overall failure. The planar failure pattern appears mainly in the specimens with $\gamma = 75°$, for example, specimens S-45-75, S-60-75, and S-75-75.

Apart from the specimens mentioned above, all the other specimens exhibit shear failure patterns. The shear failure pattern is also the most common pattern in the ubiquitous-joint specimens. Specimens S-45-60, S-60-60, S-75-30, and S-75-45 are typical examples of the shear-II failure pattern.
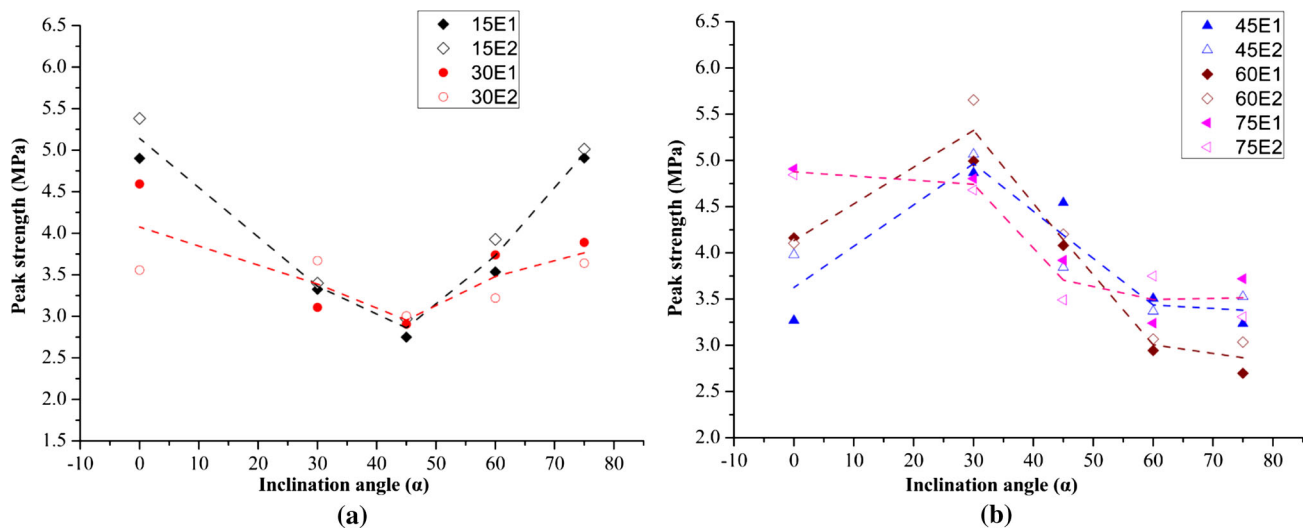
2.4 Peak Strength of the Rock-like Specimens Under Uniaxial Compressive Loads

Figure 10 shows the peak strength (UCS_J) of the multi-fissure specimens obtained from the ubiquitous-joint rock-like specimen compression tests versus α. For the specimens with $\gamma = 15°$ and $30°$ (Fig. 10a), UCS_J varies considerably as α increases from $0°$ to $75°$. For both γ values, UCS_J decreases as α increases from $0°$ to $45°$, and increases for $\alpha > 45°$.

The UCS_J values for the specimens with $\gamma = 45°$ and $60°$ (Fig. 10b) show similar tendencies when α rises from $0°$ to $75°$, increasing as α increases from $0°$ to $30°$, and decreasing for $\alpha > 30°$. When $\alpha = 30°$, the specimens (S-30-45, S-30-60) reach their peak UCS_J value. However, for the specimen with $\gamma = 75°$, the UCS_J peaks at $\alpha = 0°$ and then decreases until $\alpha = 60°$ and increases for $60° \le \alpha \le 75°$.

Table 2 Failure patterns of ubiquitous-joint rock-like specimens

γ / α	0	30	45	60	75
15	Stepped path	Stepped path	Stepped path + shear-I	Stepped path + shear-I	Shear-I
30	Stepped path	Shear-I	Shear-I	Shear-I	Shear-II
45	Shear-I	Shear-I	Shear-I	Shear-I	Shear-II
60	Shear-I	Stepped path + shear-I	Shear-II	Shear-II	Shear-I
75	Shear-I	Stepped path + shear-I	Planar	Planar	Planar

Fig. 10 Peak strengths of ubiquitous-joint rock-like specimens with different inclination angles (α)

3 Numerical Modeling and Simulated Results

3.1 PFC2D, Model Generation, and Calibration of Micro-mechanical Parameters

Itasca's upgraded version of PFC2D (based on the principle of the discrete element method) can be used to study the propagation of cracks in brittle material such as rocks, rock-like material (Lee and Jeon 2011; Yang et al. 2014; Bahaaddini et al. 2013; Wong and Zhang 2014; Fan et al. 2015 and so on), and clays (Vesga et al. 2008). In PFC2D, material is modeled as collections of particles (rigid circular disks) (Itasca Consulting Group 2002). Each particle is in contact with the neighboring particles via the contact-bond or parallel-bond model. In the parallel-bond model, the bond is depicted as a rectangle of cement-like material that can transmit both force and moment between particles (Potyondy 2007). In this model, bond breakage causes an immediate decrease in macro-stiffness because the stiffness is caused by both the contact stiffness and bond stiffness (Potyondy 2007; Cho et al. 2007). Hence, the parallel-bond model is viewed as a realistic method for modeling brittle materials and is often used to simulate crack initiation and propagation in rocks or rock-like materials (Cho et al. 2007; Lee and Jeon 2011; Yang et al. 2014; Wong and Zhang 2014; Manouchehrian and Marji 2012; Manouchehrian et al. 2014 and so on). In this study, we also use PFC2D (parallel-bond model) to carry out the numerical simulation for the ubiquitous-joint rock-like specimens under uniaxial compression.

It is very difficult to determine the micro-parameters of a material (such as the particle contact modulus, parallel-bond modulus, particle normal/shear stiffness, and the parallel-bond normal/shear strengths) based on macro-parameters such as Young's modulus, UCS, and Poisson's ratio. To better understand the effect of the micro-parameters on the PFC2D numerical results, intensive research on the relationship between the microscopic parameters and macroscopic properties of the specimens/material was carried out (Huang 1999; Potyondy and Cundall 2004; Yang et al. 2006; Cho et al. 2007; Koyama and Jing 2007; Yoon 2007). The ratio of particle normal to shear stiffness (k_n/k_s) has a considerable effect on the Young's modulus: as k_n/k_s increases, the Young's modulus decreases (Yang et al. 2006). For the UCS, it increases with the normal/ shear bond strength and friction coefficient, while it exhibited small fluctuations and had no clear trend of increasing or decreasing when k_n/k_s and E_c (contact modulus) increased (Yang et al. 2006). The Poisson's ratio is affected mainly by k_n/k_s; it increases with higher k_n/k_s (Yang et al. 2006; Yoon 2007). In this paper, the micro-parameters were determined through the trial-and-error approach, which is an accepted method (Lee and Jeon 2011; Yang et al. 2014; Ghazvinian et al. 2012; Zhang and Wong 2013a; Zhang et al. 2015a, b; Manouchehrian et al. 2014; Bahaaddini et al. 2013; Fan et al. 2015; Cao et al. 2016a, b). Although this method is not considered state of the art, it can nonetheless lead to successful results. After calibration, the micro-parameters used in this study reflect the macro-mechanical behavior of the rock-like material. Table 3 lists the micro-parameters determined in this study by a series of 'trial-and-error' processes (the calibration is performed only under consideration of compressive stress states); a comparison between the experimental and numerical results is provided in Table 4. Table 4 indicates that the simulated UCS and Young's modulus of the intact rock-like specimens are similar or equal to those obtained experimentally.

Table 3 Microscopic parameters for rock mass

Micro-parameters	Values	Remarks
Minimum mean radius (mm)	0.25	Uniform distribution
R_{max}/R_{min}	1.66	
Particle contact modulus E_c (GPa)	2.45	
Particle normal/shear stiffness	2.7	
Particle friction coefficient (μ)	0.5	
Parallel-bond modulus (GPa)	2.45	
Parallel-bond normal/shear stiffness	2.7	
Parallel-bond normal strengths, mean (MPa)	5.53	Normal distribution
Parallel-bond normal strength, SD (MPa)	0.6	10.84 % of mean value
Parallel-bond shear strengths, mean (MPa)	5.53	Normal distribution
Parallel-bond shear strength, SD (MPa)	0.6	10.84 % of mean value

Table 4 Comparison between experimental and numerical results for intact material macro-mechanical parameters

	Experimental results	Numerical results
Uniaxial compressive strength, UCS (MPa)	8.104	8.096
Young's modulus, E (GPa)	3.242	3.176
Poisson ratio	0.2371	0.2397

Previous studies (Huang 1999; Potyondy and Cundall 2004; Yang et al. 2006; Cho et al. 2007; Koyama and Jing 2007; Yoon 2007; Zhang and Wong 2013a) have considered particle size and size distribution. For example, Yang et al. (2006) systematically studied the influence of the model size (L/d) and the size of the microscopic parameters on the macroscopic properties, such as Young's modulus, Poisson's ratio, and peak strength (UCS). They pointed out that the Young's modulus showed an increase trend with rising L/d until it reached 32.5, after which the Young's modulus remained almost constant. However, the Poisson's ratio decreased with increasing L/d and become stably when L/d was larger than 32.5. The UCS was almost constant when L/d increased from 5 to 62.5. Additionally, the d_{max}/d_{min} ratios (2, 2.4, 4.2, and 6.2) were also considered and the results indicated that the particle microstructure has no considerable effect on the Young's modulus, Poisson's ratio, or UCS. Based on a fixed d_{max}/d_{min} ratio of 1.66, Potyondy and Cundall (2004) investigated the influence of particle and model size on the simulation results of Lac du Bonnet granite using PFC2D. The results indicated that the UCS and Young's modulus exhibited slight fluctuations and showed no clear trend of increasing or decreasing when the L/d ratio changed from 11 to 88, while the Poisson's ratio remained about the same. On the whole, the previous studies show that the particle microstructure configuration has only a small influence on the macroscopic deformability and strength behavior in the simulations. Further, these studies covered a wide range of L/d values, from 5 to 200, and the results indicate that the macroscopic

properties exhibit some fluctuation at low L/d values and stabilize once L/d is larger than 50. However, in this study, the mean radius was set as 0.25 mm, yielding a L/d rate of 600, which is sufficiently high to achieve a stable PFC simulation.

Figure 11 shows the numerical intact specimen generated by PFC2D. The scale of the numerical specimen is equal to that of the specimens in the experiment: 150×200 mm (width $\times$ height). The gray circles are the particles, and the fine green and pink lines represent the contacts and parallel bonds, respectively.

Usually, the micro-mechanical parameter values assigned for the particles that represent joints are smaller than those for the particles that represent intact material. In the numerical model, the joints are generated through changing the micro-mechanical parameter values of the particles on the areas of the joints. The joint-related particles are shown in white in Fig. 12.

As mentioned above, we created the joints in the rock-like specimens by inserting mica sheets during specimen production; the specimens were then removed from the mold and soaked in water for 3 days. During the curing period, the humidity was controlled at 80 %. Hence, the strength of the mica sheets is similar to that of paper. Moreover, because the mica sheet is composed of multi-layer paper-like material, after absorbing water, it separates easily during the testing. Therefore, for the micro-mechanical parameter values of the joints (Table 5), the parallel-bond normal and shear strengths were set as 0, and the other micro-mechanical parameters were also far below those of the intact material particles.

Fig. 11 Numerical intact specimen generated in PFC2D in this research
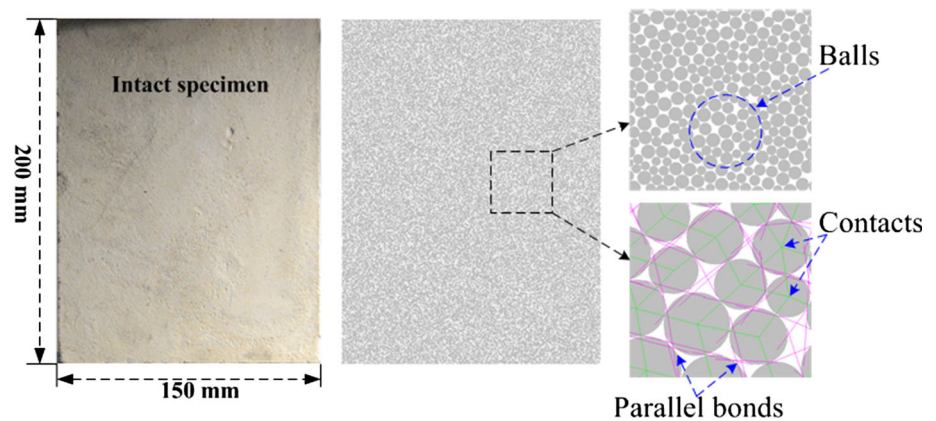
Fig. 12 Numerical specimens containing multiple joints where α is the angle of joint-1 ($\alpha = 30°$), β is the angle of joint-2, γ is angle of fissure 1 and fissure 2 ($\gamma = \beta - \alpha$, $\gamma = 15°, 30°, 45°, 60°, 75°$)
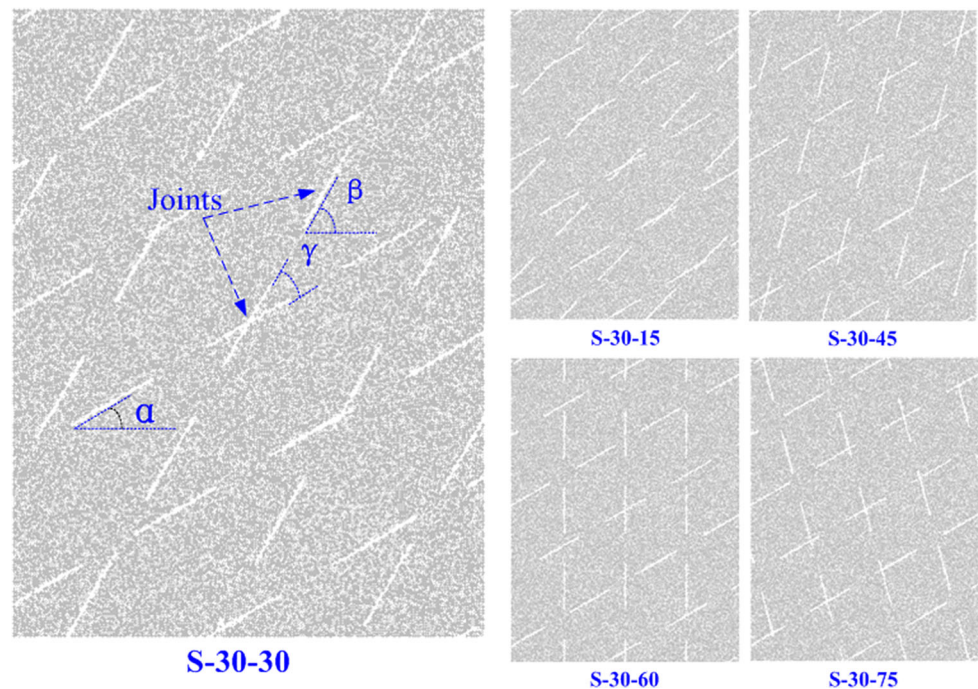
Table 5 Microscopic parameters for joints

Joint particle friction coefficient	0.08
Joint particle normal stiffness (N/m)	250
Joint particle shear stiffness (N/m)	250
Joint particle normal bond strength (MPa)	0
Joint particle shear bond strength (MPa)	0

3.2 Cracking Characteristics in Rock-like Specimens Containing Multiple Joints

As mentioned above, under uniaxial loading, there are four types of failure patterns in the ubiquitous-joint rock-like specimens. The numerical results show similar failure characteristic to the failure patterns of the experiments

(Figs. 6, 7, 8, 9). The stress–strain curve and tensile and shear bond failures were calculated for the stepped path failure (Fig. 13a), planar failure (Fig. 13b), shear-I failure (Fig. 13c), and shear-II failure pattern (Fig. 13d). The numerical result (black line) and experimental result (maroon line) are shown along with the tensile and shear bond failure curves obtained from the numerical simulation with incremental axial strain. Note that 'Crack num' stands for the total number of bond failures, 'Tensile crack' stands for the number of normal bond failures and 'Shear crack' stands for the number of shear bond failures. The crack propagation and coalescence process of the ubiquitous-joint rock-like specimens simulated by PFC2D under uniaxial compression are shown in Figs. 14, 15, 16, and 17. The failure process corresponds in sequence to points a–e on the stress–strain curve obtained from the numerical

simulation. Careful examination of all the failure patterns shows that the stress–strain curve can be divided into three stages: stage I, microscopic cracks initiation stage (from 0 to point *a*); stage II, stable cracks growth stage (from point *a* to point *c*); and stage III, macroscopic fracturing stage (from point *c* to point *e*).
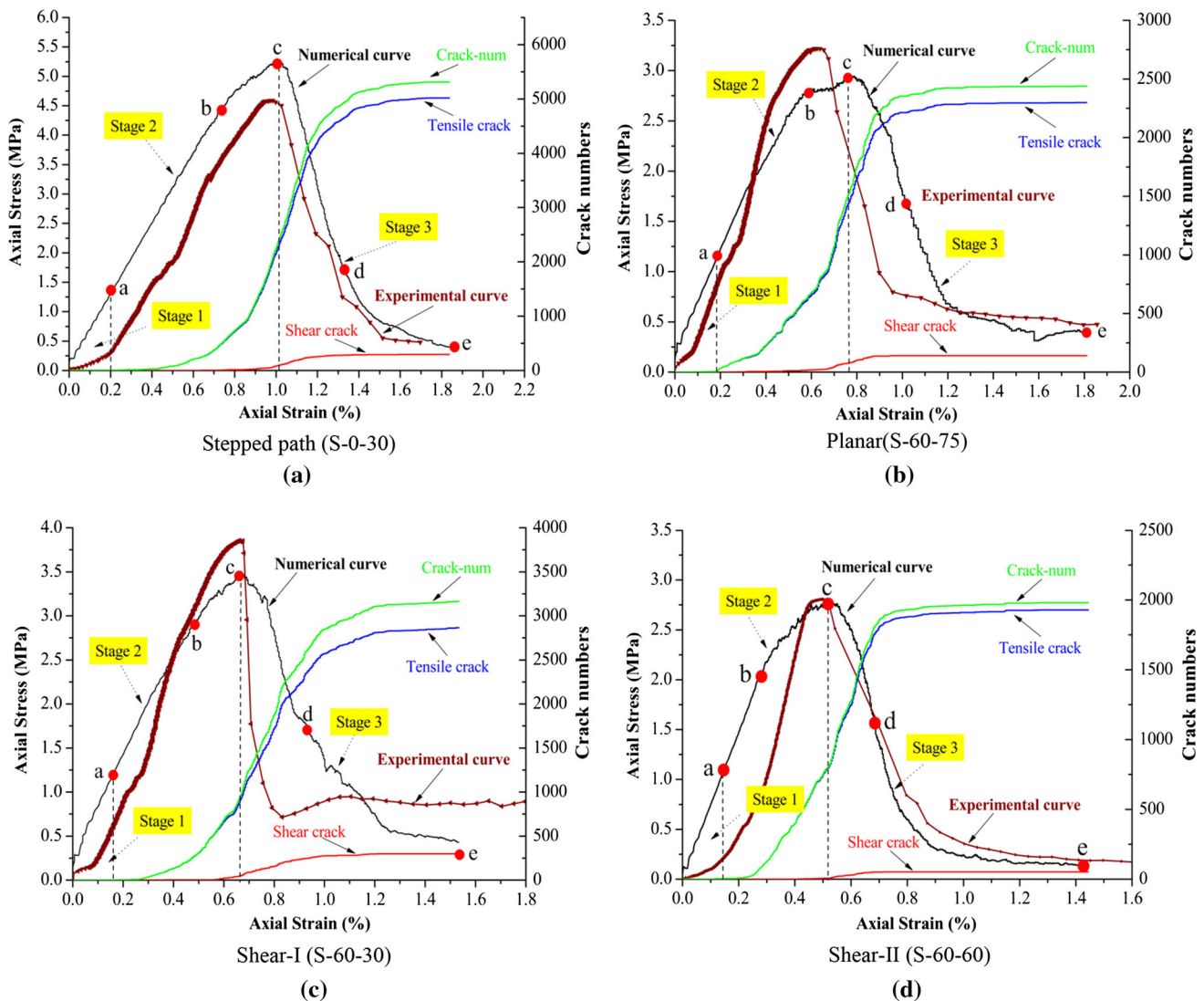
3.2.1 Stepped Path Failure

In stage 1 (Fig. 13a), the stress–strain curve shows non-linearity as the axial strain increases. After reaching the crack initiation point (point *a*), micro-cracks develop from the pre-existing flaws (Fig. 14a), and no far-field cracks appear in the specimen.

After crack initiation (point *a*), the specimen enters the second stage, the 'stable cracks growth' stage. In stage II,

only small fluctuations appear in the stress–strain curve because the micro-cracks increase stably during this stage, and some micro-cracks link to form macro-cracks. At point *b*, there are obvious wing cracks in the specimen (Fig. 14b); at the same time the axial stress reaches 84.3 % of the UCS_J.

After point *c* (Fig. 14c), the stress–strain curve drops to a low stress level, which indicates that the specimen enters the macroscopic fracturing stage. From point *c* to *e*, the bond breakages undergo accelerating growth. In Fig. 14d, the specimen undergoes macroscopic failure and there are several stepped failure planes. On the main failure plane, the pre-existing flaws link with the others through tensile cracks. During stage III, from point *d* to *e*, even though the stepped failure plane appears in the specimen, with further loading, the tensile cracks continue to propagate until reaching the residual strength.

Fig. 13 Stress–strain curve and tensile and shear bond failures for **a** stepped path failure, **b** planar failure, **c** shear-I failure, and **d** shear-II failure patterns
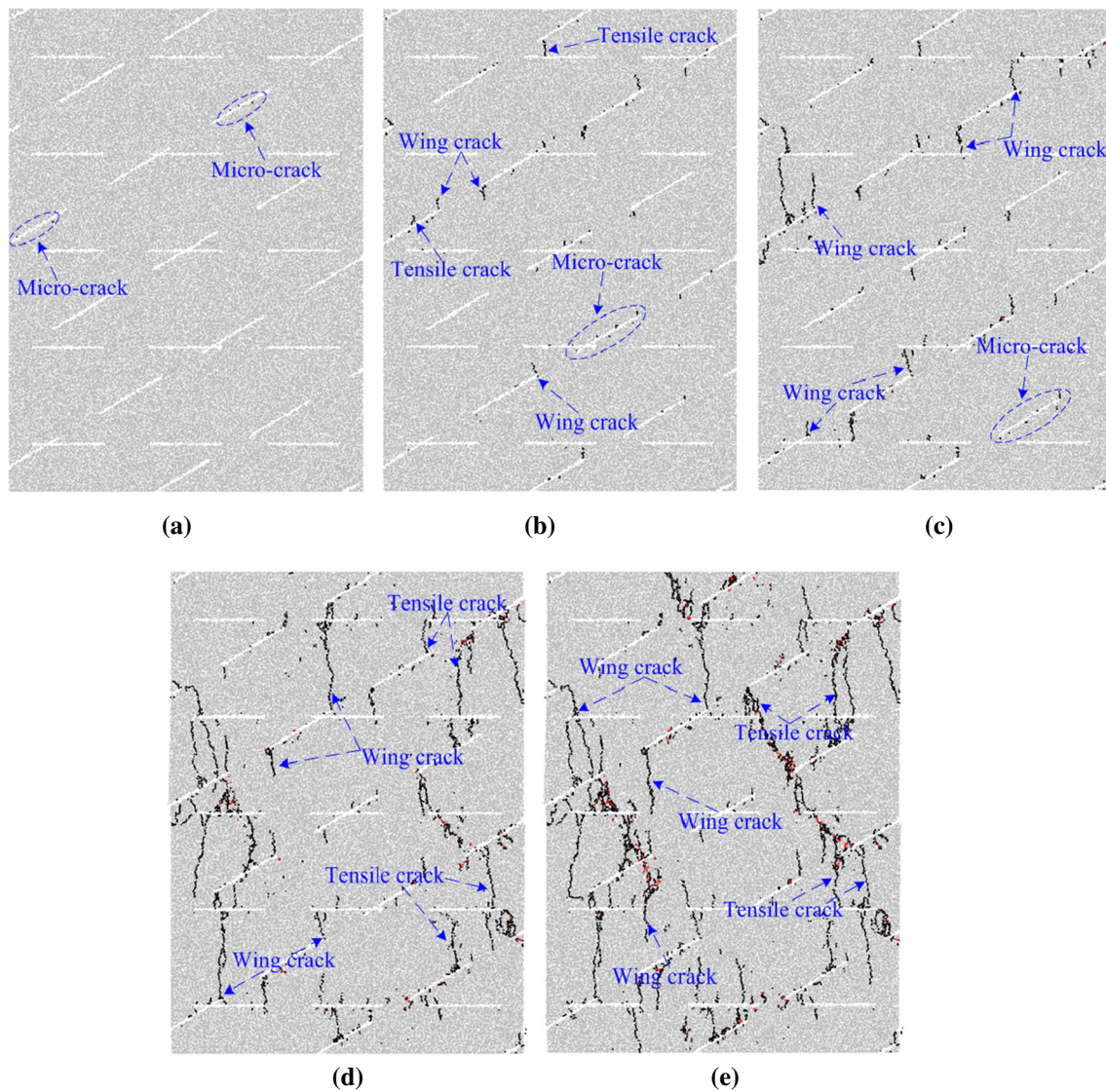
Fig. 14 Failure process at different axial strain levels for a typical stepped path failure (S-0-30) (*black lines* and *red lines* indicate normal and shear bond failures, respectively). **a** Crack initiation, **b** crack development (84.3 % peak), **c** peak strength, **d** crack coalescence (30.76 % post-peak), and **e** residual strength (7.7 % post-peak) (color figure online)
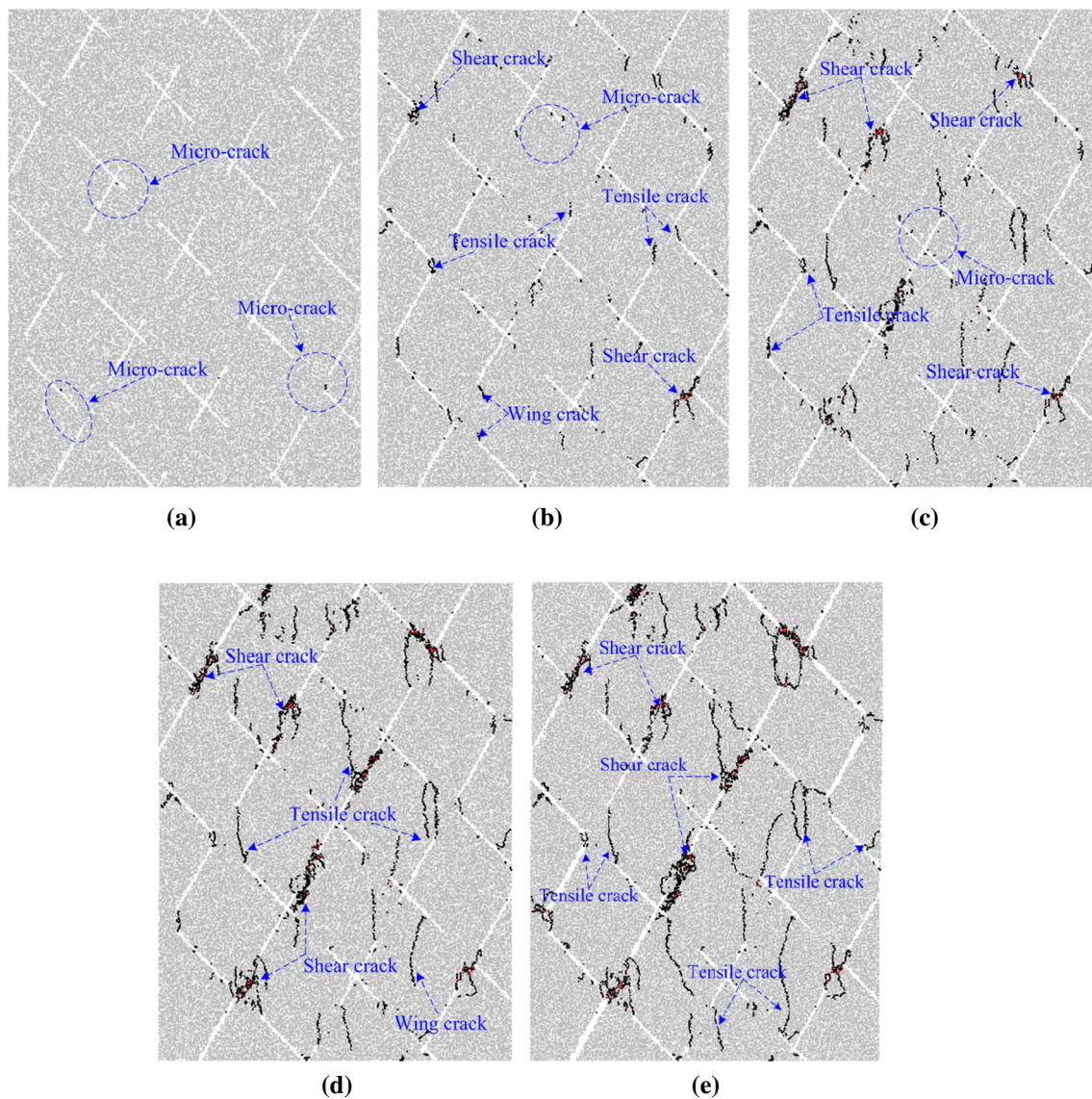
3.2.2 Planar Failure

The planar failure pattern appears mainly in the specimens with $\gamma = 75°$. The stress–strain curve and tensile/shear bond failures seen in specimen S-60-75 are typical examples of the planar failure pattern (Fig. 13b). For both specimens S-0-30 and S-60-75 (Fig. 13a, b), the numerically simulated stress–strain curve is in good agreement with the experimental curve except at the initial stage of loading.

In the numerically simulated stress–strain curve (S-60-75), there is some fluctuation between the point of origin and point c. The first micro-crack appears when the axial strain reaches 0.18 % (point a in Fig. 13b). As shown in

Fig. 15a, the micro-cracks originate from the pre-existing fissure tips. With continuous loading, at point b the micro-cracks cluster and form recognizable macro-cracks in the fissure tips, but the specimen still maintains integrity and stability as shown in Fig. 15b. At the peak stress (point c), the macro-cracks extend further (Fig. 15c), and some pre-existing flaws link with neighboring flaws via tensile or shear cracks.

In the macroscopic fracturing stage (from point c to e), for specimen S-60-75 the increase in micro-cracks is more obvious than in the microscopic cracks initiation stage (from 0 to pint a) and in stage II (the stable cracks growth stage, from point a to c). More macro-cracks can be observed as the axial strain increases. During this stage, the

Fig. 15 Failure process at different axial strain levels for a typical planar failure (S-60-75) (*black lines* and *red lines* indicate normal and shear bond failures, respectively). **a** Crack initiation, **b** crack development (93.17 % peak), **c** peak strength, **d** crack coalescence (55.7 % post-peak), and **e** residual strength (14.18 % post-peak)

micro-cracks coalesced (Fig. 15d), leading to a continuous degradation in strength (from point *c* to point *d*). After point *d*, the micro-cracks remain almost stable, and finally, the axial stress (with minor fluctuations) reaches its residual strength (Fig. 15e).

3.2.3 Shear-I

In the shear-I failure pattern, a single or a set of parallel shear failure planes appear in the specimen. Figure 13c shows the stress–strain curves of the numerical result (black line), experimental result (maroon line), and the tensile and shear bond failure curves for specimen S-60-30. As with specimens S-60-75 and S-0-30, although there is

some difference between the numerical and experimental curve, the two curves show similar tendencies.

Figure 16 shows the crack propagation and coalescence process of specimen S-60-30 as a typical example of the shear-I failure pattern. As with the stepped path and planar failure patterns, in stage I of Fig. 14c, the stress–strain curve shows nonlinearity as the axial strain increases. After the axial strain rises to 0.165 %, the specimen reaches the crack initiation point (point *a*) and micro-cracks develop from the pre-existing flaws as shown in Fig. 16a.

In the stable cracks growth stage (from point *a* to point *c*), the axial stress at point *b* is equal to 82.15 % of the UCS_J and wing cracks start to appear in the specimen as shown in Fig. 16b. With continuous loading, the micro-
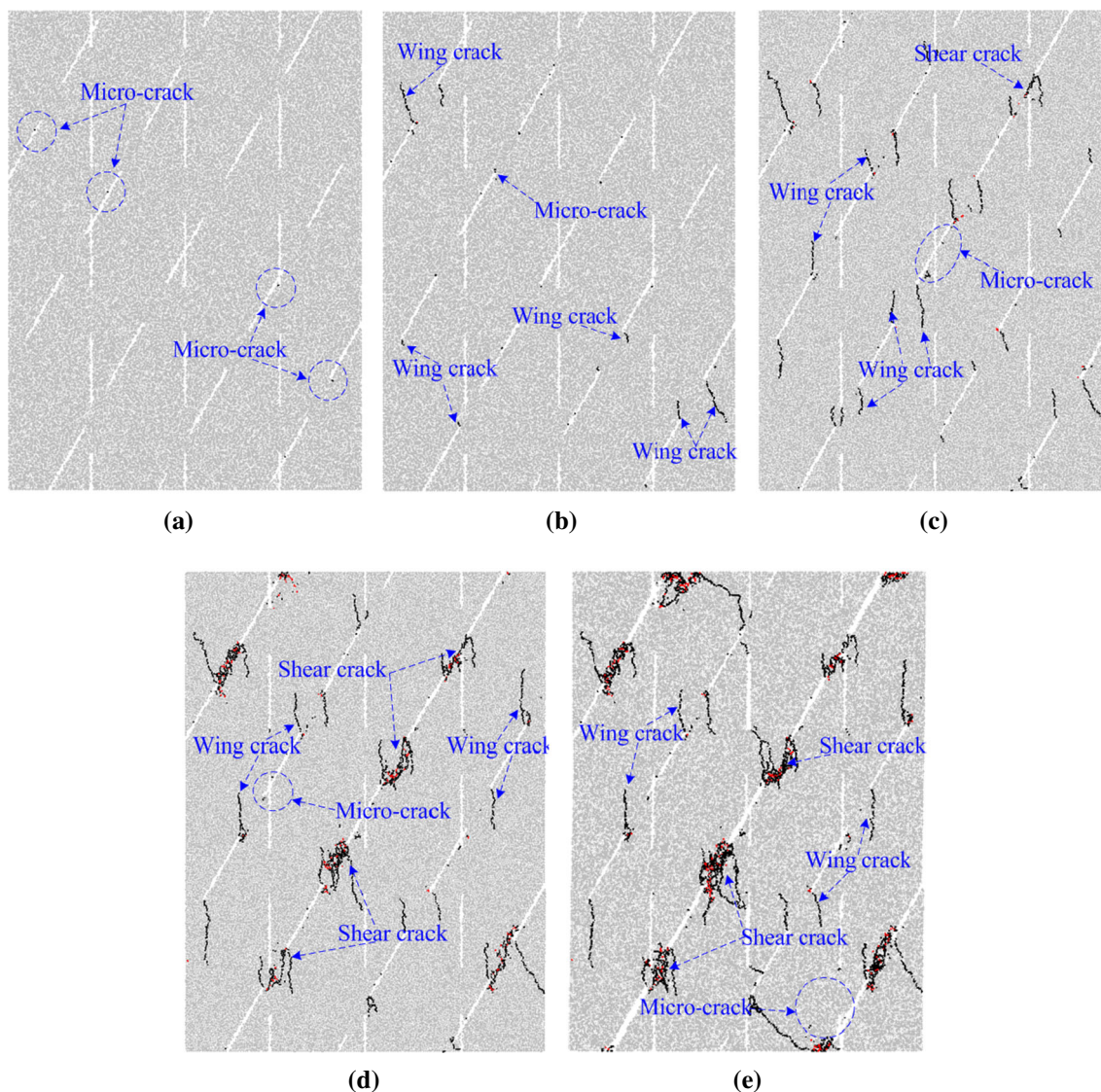
Fig. 16 Failure process at different axial strain levels for a typical shear-I failure (S-60-30) (*black lines* and *red lines* indicate normal and shear bond failures, respectively). **a** Crack initiation, **b** crack development (82.15 % peak), **c** peak strength, **d** crack coalescence (53.3 % post-peak), and **e** residual strength (11.76 % post-peak)

cracks increase stably, but the specimen is still able to maintain its mechanical integrity and stability. When the axial stress reaches the peak strength, crack coalescence occurs in the specimen as shown in Fig. 16c. Finally, the specimen enters the last stage and the micro-cracks grow rapidly. In this stage, some macro-failure appears in specimen S-60-30.

At point *d*, many pre-existing flaws coalesce as the micro-cracks combine (Fig. 16d); according to previous studies (Wong and Einstein 2009a; Sagong and Bobet 2002; Cao et al. 2016b), most of the coalescence modes between pre-existing flaws are of the quasi-coplanar secondary crack type. With further loading, the axial stress decreases with the growth of axial deformation until reaching the residual strength (Fig. 16e). Specimen S-60-

30 (Fig. 16e) was split into three blocks by the parallel shear failure plane. Generally, the simulated stress–strain curve (Fig. 13c) is similar to the experimental stress–strain curve apart from some fluctuations.

3.2.4 Shear-II

As mentioned above, in the shear-II failure pattern, the specimen contains a set of cross-shear failure surfaces. Specimen S-60-60 is a typical example of this pattern. Figure 13d depicts the stress–strain curves of the numerical result (black line), experimental result (maroon line), and the tensile and shear bond failure curves for specimen S-60-60. Figure 17 shows the crack propagation and coalescence process of specimen S-60-60, derived from
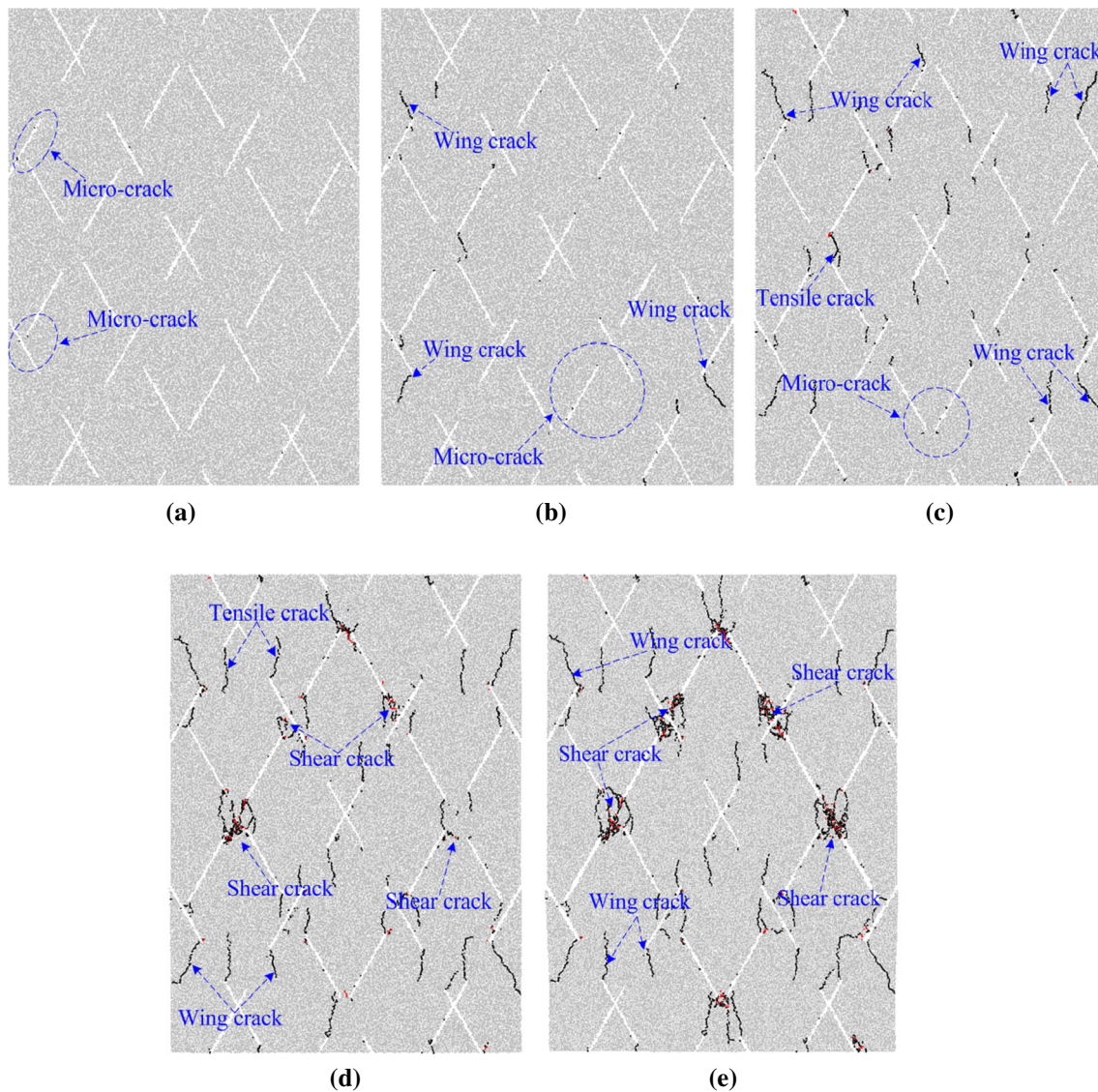
Fig. 17 Failure process at different axial strain levels for a typical shear-II failure (S-60-60) (*black lines* and *red lines* indicate normal and shear bond failures, respectively). **a** Crack initiation, **b** crack development (75.36 % peak), **c** peak strength, **d** crack coalescence (57.1 % post-peak), and **e** residual strength (7.4 % post-peak) (color figure online)

PFC2D. As in the case of specimen S-60-30, the numerically simulated stress–strain curve (black line) can be divided into three stages and it agrees well with the experimental curve (maroon line), including the post-peak region.

In stage I, the axial stress grows as the axial strain increases. When the specimen is loaded to point *a* (the axial strain equals 0.15 %), micro-cracks develop from the flaws as shown in Fig. 17a. As in the stepped path failure, planar failure, and shear-I failure patterns, at the point *a*, only some micro-cracks and no far-field cracks appear in specimen S-60-60. At point *b*, the axial stress reaches 75.36 % of the peak strength, and the wing cracks and other tensile cracks are clearly visible.

Generally, during stages I and II, the simulated stress–strain curve (Fig. 13d) is similar to the experimental stress–strain curve (maroon line) apart from some fluctuations. After the peak stress (point *c*), the axial stress drops dramatically and the specimen enters the macroscopic fracturing stage (from point *c* to point *e*). During stage III, the numerical curve looks very similar to the experimental stress–strain curve.

At point *d*, the pre-existing flaws are linked through a combination of coplanar shear cracks or mixed cracks, and many rock bridges are cut by macro-cracks; the cross-shear failure plane is obvious at point *d* (Fig. 17d). After point *d*, the axial stress continues to decrease until reaching the residual strength (Fig. 17e).

Notably, as shown in Fig. 13, there is axial stress at zero axial strain. This phenomenon can be explained as follows: In PFC2D, the rock-like material is modeled as collections of particles (rigid circular disks). In order to make each particle contact with their neighboring particles, we have to input a locked-in stress during the process of model generation, and in this research, the locked-in stress value is 0.1 MPa. Therefore, in the numerical curves (Fig. 13), there is axial stress around 0.1 MPa at zero axial strain.

In addition, the rock specimen at the pre-peak stage in numerical simulations (Fig. 13c, d) seems to have a softer response than that in experiments, which is caused by the following reasons. The stress–strain curves of the specimens exhibit significant nonlinear characteristics, rendering it difficult to determine the Young's modulus of the rock-like specimen. So the Young's modulus was taken as the secant modulus in this research. During the calibration process, the numerical property was also determined in this way. At the same time, two other reasons may also contribute to this phenomenon: (1) the imbalance in the curing will have an effect on the mechanical properties of specimens, and (2) the PFC2D analysis is in two dimensions, while the characteristics measured in the rock-like specimens are three-dimensional.

3.3 Comparison Between the Experimental and Numerical Results

Figure 18 shows the peak failure stresses in the ubiquitous-joint rock-like specimens derived from the numerical simulations and laboratory experiments. Figure 18a–e shows that the numerical results have a similar trend to the experimental results. In the numerical simulation, for intersection angles of 15° and 30°, the peak strength of the specimens decreases, while α increases from 0° to 45° but increases when α widens from 45° to 75°. This trend matches the observation in the experiments.

For the specimens with $\gamma = 45°$ and 60° and $0° \leq \alpha \leq 60°$, the numerical result shows similar trends with increasing α. The specimens (S-30-45, S-30-60) obtain the highest UCS$_J$ value when $\alpha = 30°$. However, for $\gamma = 75°$ the UCS$_J$ is highest when $\alpha = 0°$ and decreases until $\alpha = 45°$. For $45° \leq \alpha \leq 75°$, the simulated UCS$_J$ value rises with increasing α. The experimental and numerical results show similar UCS$_J$ trends for the specimens with $\gamma = 45°$, 60°, and 75°.

As mentioned above, the peak failure stresses of the numerical and experimental results show a similar trend, but also some differences. This may be due to imbalances in the curing and the heterogeneity of the specimens.

Figures 19, 20, 21, and 22 show the four typical failure modes obtained by PFC2D and the corresponding failure modes obtained for the same specimens in the rock-like material experiments. The numerical results compare quite well with the experimental results. For the stepped path failure pattern (S-0-15 and S-0-30) (Fig. 19), the overall failure of the specimen is caused by the propagation of tensile cracks. Notably, micro-cracks that appear in various locations in the numerical specimen cannot be observed by the naked eye in the experiment.

Figure 20 shows a comparison of the numerical and experimental results for the planar failure pattern specimen. In both the numerical and experimental results, most of the pre-existing flaws in the specimens are connected to neighboring flaws via tensile cracks or shear cracks. Thus, the specimen is cut into many blocks by pre-existing flaws and new cracks; this is the main characteristic of the planar failure pattern.

Comparisons between the numerical and experimental results of typical shear-I and shear-II failure patterns are shown in Figs. 21 and 22, respectively. In Fig. 21, for specimen S-60-30, the shear band is near the diagonal line; two similar shear bands can be observed in specimen S-75-15. The numerical results of the shear-I failure pattern compare quite well to the experimental results. In Fig. 22, although some of the blocks fell outside the specimen, the 'cross-shear failure plane' in the experimental result is very clear and agrees well with the numerical specimens.

4 Conclusions

Combined with the laboratory tests of rock-like material and numerical simulation (PFC2D), the peak strength, crack propagation, coalescence, and failure patterns of ubiquitous-joint specimens under uniaxial loading were investigated in this study. From the simulated and experimental results, the following conclusions can be drawn:

1. Under compression, tensile cracks or shear cracks will propagate and link with other cracks to form penetration. As loading continues, the pre-existing flaws link with neighboring cracks to form various types of failure patterns. The failure patterns of ubiquitous-joint rock-like specimens can be generally classified into four categories: (1) stepped path failure, (2) planar failure, (3) shear-I failure, and (4) shear-II failure.

2. The failure patterns of rock-like specimens are affected by the joint-1 inclination angle (α) and intersection angle (γ). Specimens S-0-15, S-0-30, and S-30-15 exhibited a stepped path failure pattern; the failure of these specimens was caused mainly by the propagation of tensile cracks. The planar failure pattern appears mainly in the specimens with $\gamma = 75°$ such as specimens S-45-75, S-60-75, and S-75-75. The shear
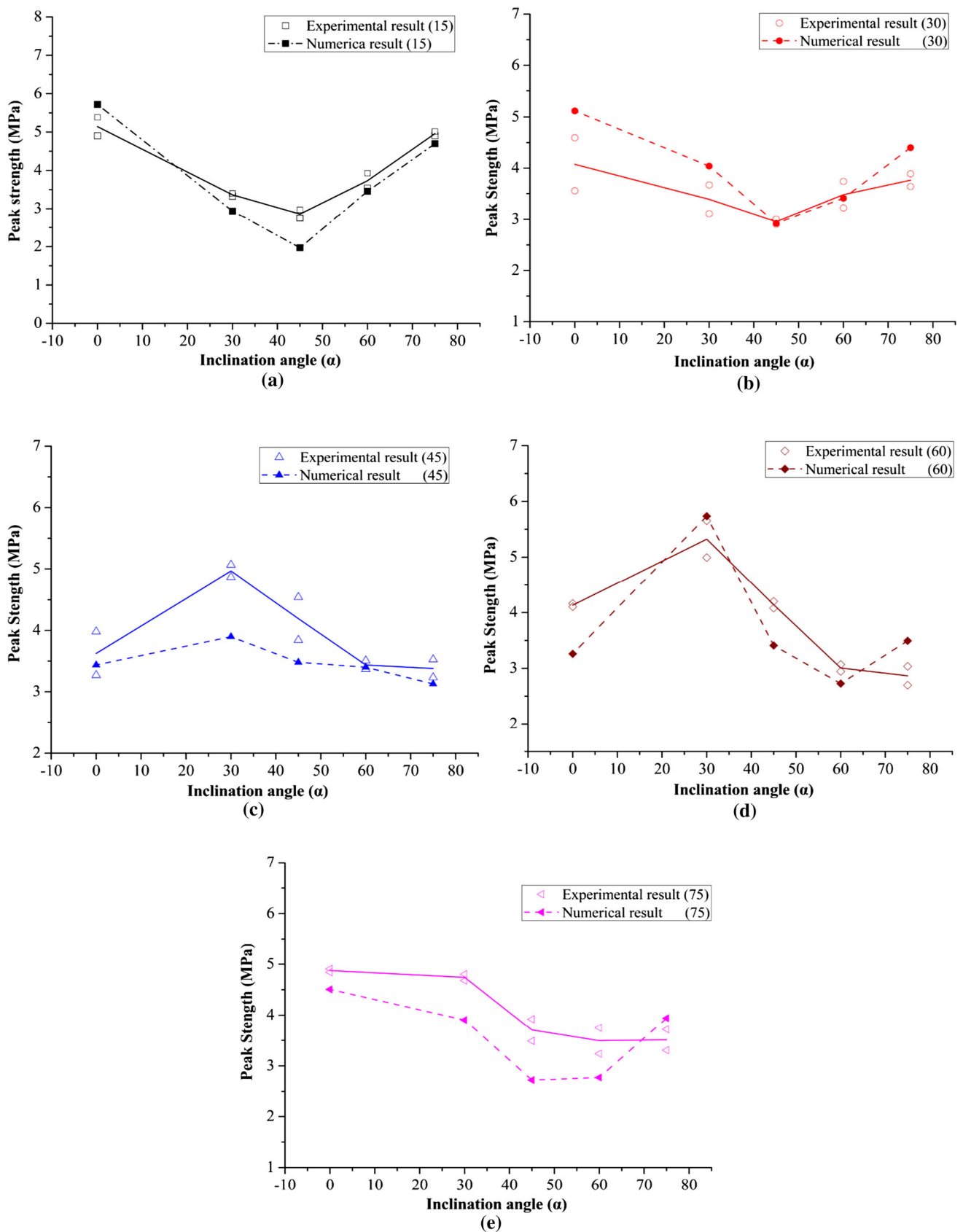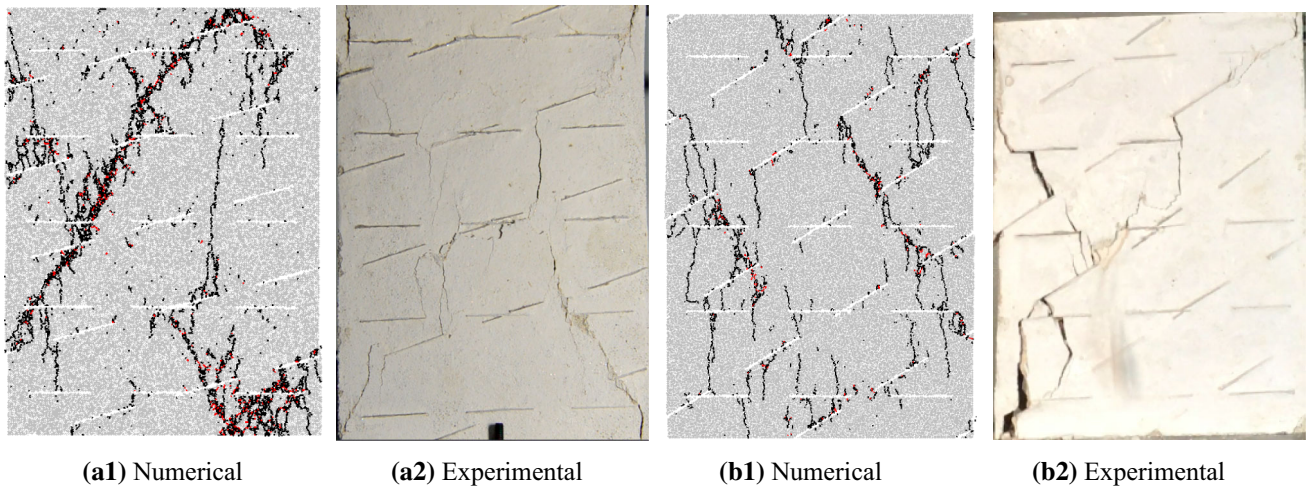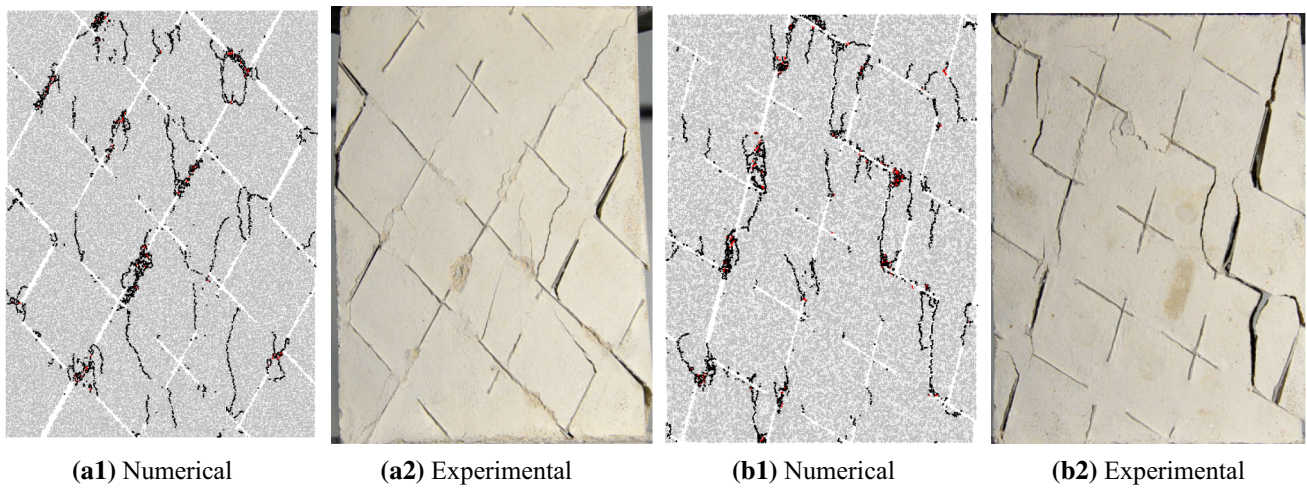
Fig. 18 Effect of joint-1 inclination angle α and intersection angle γ on UCS$_J$

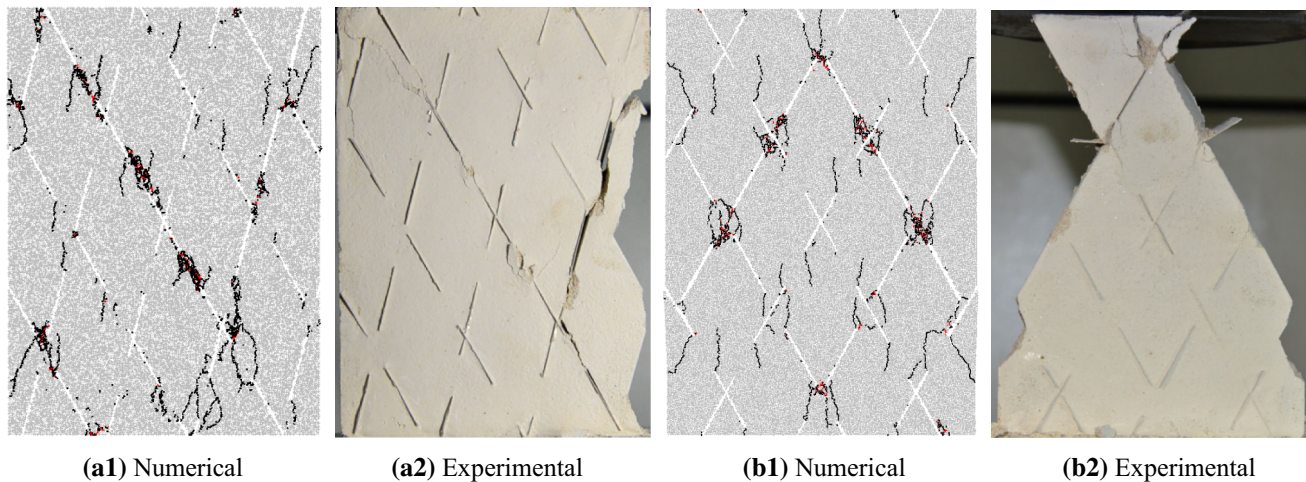**(a1)** Numerical   **(a2)** Experimental   **(b1)** Numerical   **(b2)** Experimental

Fig. 19 Stepped path failure mode comparisons between experimental and numerical results: **a** S-0-15; **b** S-0-30

(a1) Numerical   **(a2)** Experimental   **(b1)** Numerical   **(b2)** Experimental

Fig. 20 Planar failure mode comparisons between experimental and numerical results: **a** S-60-75; **b** S-75-75

(a1) Numerical   **(a2)** Experimental   **(b1)** Numerical   **(b2)** Experimental
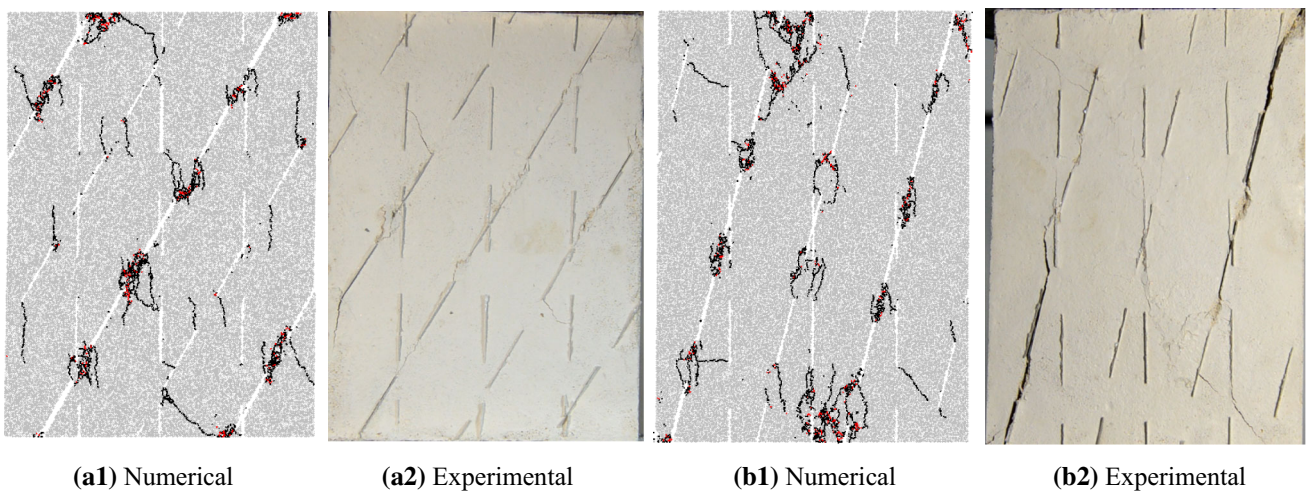
Fig. 21 Shearing-I failure mode comparisons between experimental and numerical results: **a** S-60-30; **b** S-75-15

(a1) Numerical   **(a2)** Experimental   **(b1)** Numerical   **(b2)** Experimental

Fig. 22 Shearing-II failure mode comparisons between experimental and numerical results: **a** S-75-45; **b** S-60-60

failure pattern is the most common failure pattern in the ubiquitous-joint specimens. Specimens S-45-60, S-60-60, S-75-30, and S-75-45 are typical examples of the shear-II failure pattern.

3. The joint-1 inclination angle α has a very high influence on UCS_J, and the strength of the ubiquitous-joint rock-like specimens showed different tendencies when α varied from 0° to 75°. The UCS_J values of specimens with $\gamma = 15°$ and 30° show similar trends when α changes from 0° to 75°: decreasing as α increases from 0° to 45° and increasing as α increases from 45° to 75°. The UCS_J values for specimens with $\gamma = 45°$ and 60° show similar trends when α changes from 0° to 75°. In contrast, for specimens with $\gamma = 45°$ or 60°, the UCS_J increases as α increases from 0° to 30° and decreases when α rises from 30° to 75°. For specimens with $\gamma = 75°$, the highest UCS_J value occurs when $\alpha = 0°$, while when α increases from 60° to 75°, the UCS_J value increases.

References

Bahaaddini M, Sharrock G, Hebblewhite BK (2013) Numerical investigation of the effect of joint geometrical parameters on the mechanical properties of a non-persistent jointed rock mass under uniaxial compression. Comput Geotech 49:206–225

Bobet A (2000) The initiation of secondary cracks in compression. Eng Fract Mech 66:187–219

Bobet A, Einstein HH (1998a) Fracture coalescence in rock-type materials under uniaxial and biaxial compression. Int J Rock Mech Min Sci 35(7):863–888

Bobet A, Einstein HH (1998b) Numerical modeling of fracture coalescence in a model rock material. Int J Fract 92(3):221–252

Bombolakis EG (1968) Photoelastic study of initial stages of brittle fracture in compression. Tectonophysics 6(6):461–473

Cao P, Liu T, Pu C, Lin H (2015) Crack propagation and coalescence of brittle rock-like specimens with pre-existing cracks in compression. Eng Geol 187(17):113–121

Cao W, Li X, Tao M, Zhou Z (2016a) Vibrations induced by high initial stress release during underground excavations. Tunn Undergr Space Technol 53:78–95

Cao R, Cao P, Lin H, C Pu, K Ou (2016b) Mechanical behavior of brittle rock-like specimens with pre-existing fissures under uniaxial loading: experimental studies and particle mechanics approach. Rock Mech Rock Eng 49(3):763–783

Cho N, Martin C, Sego D (2007) A clumped particle model for rock. Int J Rock Mech Min Sci 44(7):997–1010. doi:10.1016/j.ijrmms.2007.02.002

Dyskin AV, Sahouryeh E, Jewell RJ (2003) Influence of shape and locations of initial 3-D cracks on their growth in uniaxial compression. Eng Fract Mech 70(15):2115–2136

Fan X, Kulatilake PHSW, Chen X (2015) Mechanical behavior of rock-like jointed blocks with multi-non-persistent joints under uniaxial loading: a particle mechanics approach. Eng Geol 190(14):17–32

Ghazvinian A, Sarfarazi V, Schubert W (2012) A study of the failure mechanism of planar non-persistent open joints using PFC2D. Rock Mech Rock Eng 45:677–693

Hoek E, Bieniawski ZT (1965) Brittle fracture propagation in rock under compression. Int J Fract 1(3):137–155

Huang H (1999) Discrete element modeling of tool-rock interaction. Ph.D. thesis, University of Minnesota, Minneapolis, MN

Itasca Consulting Group (2002) Users' manual for particle flow code in 2 dimensions (PFC2D). Version 3.1. Minneapolis, Minnesota

Koyama T, Jing L (2007) Effects of model scale and particle size on micro-mechanical properties and failure processes of rocks—a particle mechanics approach. Eng Anal Bound Elem 31(5):458–472. doi:10.1016/j.enganabound.2006.11.009

Lee H, Jeon S (2011) An experimental and numerical study of fracture coalescence in pre-cracked specimens under uniaxial compression. Int J Solids Struct 48(6):979–999

Li YP, Chen LZ, Wang YH (2005) Experimental research on pre-cracked marble under compression. Int J Solids Struct 42(9/10):2505–2516

Manouchehrian A, Marji MF (2012) Numerical analysis of confinement effect on crack propagation mechanism from a flaw in a pre-cracked rock under compression. Acta Mech Sin 28(5):1389–1397

Manouchehrian A, Sharifzadeh M, Marji MF, Gholamnejad J (2014) A bonded particle model for analysis of the flaw orientation effect on crack propagation mechanism in brittle materials under compression. Arch Civ Mech Eng 14(1):40–52

Park NS (2001) Crack propagation and coalescence in rock under uniaxial compression. Master's Thesis, Seoul National University

Park CH, Bobet A (2009) Crack coalescence in specimens with open and closed flaws: a comparison. Int J Rock Mech Min Sci 46(5):819–829

Park CH, Bobet A (2010) Crack initiation, propagation and coalescence from frictional flaws in uniaxial compression. Eng Fract Mech 77(14):2727–2748

Potyondy DO (2007) Simulating stress corrosion with a bonded-particle model for rock. Int J Rock Mech Min Sci 44(5):677–691

Potyondy DO, Cundall PA (2004) A bonded-particle model for rock. Int J Rock Mech Min Sci 41(8):1329–1364

Reyes O, Einstein HH (1991) Failure mechanisms of fractured rock—a fracture coalescence model. In: Proceedings of 7th congress of the ISRM, Aachen, Germany, pp 333–340

Sagong M, Bobet A (2002) Coalescence of multiple flaws in a rock-model material in uniaxial compression. Int J Rock Mech Min Sci 39(2):229–241

Sahouryeh E, Dyskin AV, Germanovich LN (2002) Crack growth under biaxial compression. Eng Fract Mech 69(18):2187–2198

Shen B (1995) The mechanism of fracture coalescence in compression experimental study and numerical simulation. Eng Fract Mech 51(1):73–85

Tang CA, Lin P, Wong RHC, Chau KT (2001) Analysis of crack coalescence in rock-like materials containing three flaws—part II: numerical approach. Int J Rock Mech Min Sci 38(7):925–939

Vallejo LE (1987) The influence of fissures in a stiff clay subjected to direct shear. Geotechnique 37(1):69–82

Vallejo LE (1988) The brittle and ductile behaviour of clay samples containing a crack under mixed-mode loading. Theor Appl Fract Mech J 10:3–78

Vallejo LE (1989) Fissure parameters in stiff clays under compression. J Geotech Eng ASCE 115(9):1303–1317

Vallejo LE, Shettima M, Alaasmi A (2013) Unconfined compressive strength of brittle material containing multiple cracks. Int J Geotech Eng 7(3):318–322

Vasarhelyi B, Bobet A (2000) Modeling of crack initiation, propagation and coalescence in uniaxial compression. Rock Mech Rock Eng 33:119–139

Vesga LF, Vallejo LE, Lobo-Guerrero S (2008) DEM analysis of the crack propagation in brittle clays under uniaxial compression tests. Int J Numer Anal Meth Geomech 32(11):1405–1415

Wong NY (2008) Crack coalescence in molded gypsum and Carrara marble (Ph.D.) Massachusetts Institute of Technology

Wong RHC, Chau KT (1998) Crack coalescence in a rock-like material containing two cracks. Int J Rock Mech Min Sci 35(2):147–164

Wong LNY, Einstein HNY (2006) Fracturing behavior of prismatic specimens containing single flaws. In: Golden rocks 2006, the 41st US symposium on rock mechanics (USRMS)

Wong LNY, Einstein HH (2009a) Crack coalescence in molded gypsum and Carrara marble: part 1. Macroscopic observations and interpretation. Rock Mech Rock Eng 42(3):475–511

Wong LNY, Einstein HH (2009b) Crack coalescence in molded gypsum and Carrara marble: part 2. Microscopic observations and interpretation. Rock Mech Rock Eng 42(3):513–545

Wong LNY, Li HQ (2013) Numerical study on coalescence of two pre-existing coplanar flaws in rock. Int J Solids Struct 50(22–23):3685–3706

Wong LNY, Zhang X-P (2014) Size effects on cracking behavior of flaw-containing specimens under compressive loading. Rock Mech Rock Eng 47(5):1921–1930

Wong RHC, Chau KT, Tang CA, Lin P (2001) Analysis of crack coalescence in rock-like materials containing three flaws—part I: experimental approach. Int J Rock Mech Min Sci 38(7):909–924

Xie Y, Cao P, Liu J, Dong L (2016) Influence of crack surface friction on crack initiation and propagation: a numerical investigation based on extended finite element method. Comput Geotech 74:1–14

Yang SQ (2011) Crack coalescence behavior of brittle sandstone samples containing two coplanar fissures in the process of deformation failure. Eng Fract Mech 78:3059–3081. doi:10.1016/j.engfracmech.2011.09.002

Yang B, Jiao Y, Lei S (2006) A study on the effects of microparameters on macroproperties for specimens created by bonded particles. Eng Comput 23(6):607–631

Yang SQ, Yang DS, Jing HW, Li YH, Wang SY (2012) An experimental study of the fracture coalescence behaviour of brittle sandstone specimens containing three fissures. Rock Mech Rock Eng 45(4):563–582

Yang S-Q, Liu X-R, Jing H-W (2013) Experimental investigation on fracture coalescence behavior of red sandstone containing two unparallel fissures under uniaxial compression. Int J Rock Mech Min Sci 63:82–92

Yang S-Q, Huang Y-H, Jing H-W, Liu X-R (2014) Discrete element modeling on fracture coalescence behavior of red sandstone containing two unparallel fissures under uniaxial compression. Eng Geol 178:28–48

Yoon J (2007) Application of experimental design and optimization to PFC model calibration in uniaxial compression simulation. Int J Rock Mech Min Sci 44:871–889

Zhang X-P, Wong LNY (2013a) Crack initiation, propagation and coalescence in rocklike material containing two flaws: a numerical study based on bonded-particle model approach. Rock Mech Rock Eng 46:1001–1021

Zhang X-P, Wong LNY (2013b) Loading rate effects on cracking behavior of flaw contained specimens under uniaxial compression. Int J Fract 180:93–110. doi:10.1007/s10704-012-9803-2

Zhang K, Cao P, Ma G et al (2015a) Strength, fragmentation and fractal properties of mixed flaws. Acta Geotech. doi:10.1007/s11440-015-0403-y

Zhang X-P, Liu Q, Wu S, Tang X (2015b) Crack coalescence between two non-parallel flaws in rock-like material under uniaxial compression. Eng Geol 199(2015):74–90

Zhou XP, Yang HQ (2007) Micromechanical modeling of dynamic compressive responses of mesoscopic heterogenous brittle rock. Theor Appl Fract Mech 48:1–20. doi:10.1016/j.tafmec.2007.04.008

Zhou XP, Cheng H, Feng YF (2014) An experimental study of crack coalescence behaviour in rock-like materials containing multiple flaws under uniaxial compression. Rock Mech Rock Eng 47:1961–1986. doi:10.1007/s00603-013-0511-7

Zhou XP, Bi J, Qian QH (2015) Numerical simulation of crack growth and coalescence in rock-like materials containing multiple pre-existing flaws. Rock Mech Rock Eng 48:1097–1114. doi:10.1007/s00603-014-0627-4